A Geometric-Electronic Principle for Curvature-Driven Catalysis

Meijie Wang,[†] Yuxing Lin,[†] Zhulin Huang,[†] Yang Sun,[†] Shunqing Wu,[†] and Xinrui Cao[*,†,‡]

†*Department of Physics, Xiamen University, Xiamen 361005, China*

‡*Fujian Provincial Key Laboratory of Theoretical and Computational Chemistry, Xiamen University, Xiamen 361005, China*

E-mail: xinruicao@xmu.edu.cn

Abstract

Substrate curvature offers a powerful handle for tuning catalysis, yet a general quantitative framework for arbitrary anisotropic morphologies remains lacking. Here, by combining differential geometry with a symmetry-constrained Taylor expansion, we derive a geometric descriptor, φ, from the full curvature tensor that compresses complex local curvature into a predictive variable for catalytic properties. Using Fe–N_4–C single-atom catalysts as a model for CO_2RR, systematic calculations across 602 nonequivalent curved sites reveal that the curvature-dependent activity variation is governed by the out-of-plane d-orbital centroid, $\langle z \rangle$. This electronic descriptor captures the asymmetric polarization of d orbitals along the surface normal and naturally distinguishes convex from concave active sites. We trace this electronic polarization to its mechanical origin: the intrinsic stiffness contrast between pentagonal and hexagonal rings converts geometric strain into opposite vertical displacements of the metal center that drive the orbital response. This establishes a quantitative causal pathway

from geometry (φ) through mechanics and electronic structure ($\langle z \rangle$) to catalytic activity. This framework elevates local curvature from a qualitative structural feature to a quantitative and tunable design axis for catalyst engineering.

Keywords

First-principles calculations, Curvature Effect, Descriptors, M–N–C, CO_2 Reduction Reaction

Introduction

In the pursuit of tailored functionality, surface curvature has emerged as a fundamental yet underutilized physical dimension,[1,2] offering a design avenue strictly orthogonal to conventional chemical composition tuning.[3–8] This geometric modulation constitutes a universal principle that transcends material classes, spanning from the pre-organized, concave pockets of metalloenzymes[9,10] to the continuously deformable topologies of two-dimensional materials, which can host spherical,[11] cylindrical,[12] and saddle-shaped geometries.[13–15] In this landscape, harnessing substrate curvature represents a transformative strategy to precision-engineer single-atom catalysts (SACs). Given that SACs are predominantly anchored on flexible 2D scaffolds with active sites strictly governed by their local coordination environment,[16–18] curvature serves as a potent lever to modulate lattice strain[19,20] and fine-tune their electronic properties.[21]

Despite this profound impact, establishing a quantitative, predictive principle that links this tensor geometry to catalytic performance remains an elusive challenge. Experimentally, realistic supports exhibit morphological non-uniform landscapes with broad curvature distributions.[22–29] Catalytic measurements inevitably yield convoluted ensemble averages, making it nearly impossible to deconstruct and isolate the specific contributions of distinct geometric features. Theoretically, current interpretations are largely based on idealized, uniaxial

bending models (e.g., carbon nanotubes (CNTs)[30–41]) or isotropic models (e.g., spherical carbon[28,29]). While these approaches capture a linear dependence of binding strength on curvature magnitude, they fundamentally overlook the complex biaxial and anisotropic topologies inherent to realistic surfaces.[28] In addition, the vectorial nature of the electronic response induced by curvature (e.g., the inequivalence of convex and concave sides) often confounds conventional scalar descriptors (e.g., the *d*-band center), which are incapable of resolving such directionality. Even for convex surfaces, reported findings are inconsistent: while some studies report that increasing curvature strengthens adsorption,[39] others observe the exact opposite trend[36–38] under seemingly similar conditions. This inconsistency strongly suggests that interpretations relying solely on simplified geometric models (i.e., scalar curvature magnitude) are insufficient to capture the intrinsic complexity of real and anisotropic environments. Collectively, these challenges call for a universal framework that quantitatively links local tensor geometry to catalytic activity.

Herein, we establish a unified geometric–electronic framework that addresses these challenges by defining a structure–electronics–activity causal chain (Figure 1). Grounded in differential geometry, the local curvature at the active site in M–N–C is parameterized by a quadratic paraboloid defined by principal curvatures (k_1, k_2) and orientation (θ). The curvature tensor is then decomposed into three orthogonal modes—isotropic (K_i), anisotropic (K_a), and torsional (K_t). For the M–N_4 motif, point-group selection rules remove odd-order K_t terms; under the small-curvature linear approximation, this reduces to $\varphi = c_i K_i + c_a K_a$. Using Fe–$N_4$–C as a model system with 602 non-equivalent curved sites, we show that an intrinsic stiffness contrast between pentagonal and hexagonal rings converts geometric strain into opposite vertical displacements of the metal center. This mechanical response induces asymmetric out-of-plane *d*-orbital polarization, captured by the *z*-centroid descriptor ($\langle z \rangle$), and links Geometry (φ) $\rightarrow$ Mechanics $\rightarrow$ Electronics ($\langle z \rangle$) $\rightarrow$ Activity ($\Delta G_{\max}$), producing a predictive volcano relation for CO_2 reduction reaction (CO_2RR). The framework is further validated across metal centers, adsorbates, coordination environments, and periodic mod-

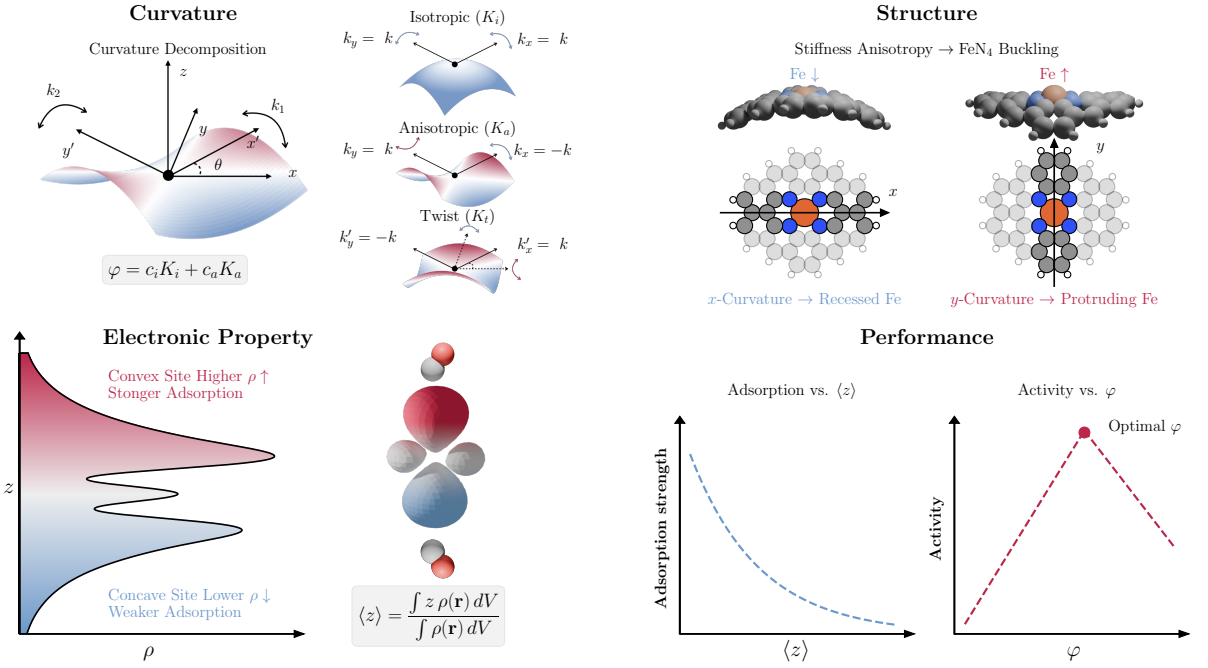

Figure 1: Curvature–structure–electronic coupling governing catalytic behavior. Local surface curvature, decomposed into isotropic (K_i), anisotropic (K_a), and twisting (K_i) modes, defines the geometric descriptor φ. The intrinsic stiffness contrast translates geometric curvature into directional buckling of the Fe–N_4 center, generating the asymmetric out-of-plane d-orbital polarization. This electronic response directly modulates adsorption energetics, establishing a volcano relationship between φ and catalytic performance.

els, and remains robust under applied electrochemical-potential conditions, supporting local curvature as a quantitative catalyst-design axis.

Computational Details

All spin-polarized DFT calculations were performed using the Vienna Ab initio Simulation Package (VASP).[42,43] The projector augmented wave (PAW) method[44] was employed to describe the ion-electron interactions. To better describe the adsorption properties on the surface, the revised Perdew-Burke-Ernzerhof[45] (RPBE) generalized gradient approximation[46] (GGA) functional was used for the exchange-correlation energy. The van der Waals interactions were accounted for using the DFT-D3 correction by Grimme.[47,48] A plane-wave cutoff energy of 500 eV was used. All structural models were placed in a supercell with dimensions of $24 \times 22 \times 16$ Å to minimize interactions between periodic images. Due to the

large size of the supercell, the Brillouin zone was sampled using a Γ-centered $1 \times 1 \times 1$ k-point mesh. The convergence criteria for electronic self-consistency and ionic relaxation were set to 10^{-5} eV and 0.02 eV/Å, respectively. In all calculations, a Hubbard-U parameter[49] of U_{eff} = 2.0 eV was applied to the Fe $3d$ orbitals, consistent with previous benchmark studies.[50,51]

To take into account the effects of solvation and applied potentials on the reaction free energies, we employed the nonlinear, nonlocal implicit solvation model as implemented in the VASPsol++ package.[52] An aqueous electrolyte with a concentration of 1.0 M was modeled using an effective ionic radius of 4.0 Å. Constant potential calculations were performed to model the system under an applied bias within the grand canonical ensemble. Based on recent benchmarks for the RPBE functional using nonlocal solvation models,[53] the absolute potential of the Standard Hydrogen Electrode (SHE) was taken as -4.44 eV relative to the vacuum level. Accordingly, to simulate an applied potential of $U = -0.8$ V vs. SHE, the Fermi level reference parameter was set to -3.64 eV. The Gibbs free energy change (ΔG) for each elementary step of CO_2RR was computed as follows:

$$\Delta G = \Delta E + \Delta E_{\text{ZPE}} - T\Delta S \tag{1}$$

where ΔE is the difference in the grand canonical potential between the adsorbed state and the reference state at a fixed potential. The zero-point energy correction (ΔE_{ZPE}) and entropy contributions ($T\Delta S$) were obtained from vibrational frequency calculations. To account for the systematic errors of the RPBE functional in describing the gas-phase CO_2 molecule, a correction of +0.45 eV was applied to its total energy, following the standard correction scheme established by Nørskov et al.[54,55] Crystal Orbital Hamilton Population (COHP) and integrated COHP (ICOHP) analyses were performed using the LOBSTER package[56,57] to quantify the intrinsic bond strengths between the first and second coordination shells along the pentagonal and hexagonal ring directions. Post-processing of the calculated data was facilitated by the VASPKIT code.[58]

Results and Discussion

Theoretical Framework

To rigorously quantify the geometric influence, we leverage the formalism of differential geometry to construct a unified theoretical framework (see Note S1 for complete derivation). The local topology of any smooth curved surface can be approximated by a quadratic paraboloid:

$$z(x,y) = -\frac{1}{2}\left[k_1\left(x\cos\theta + y\sin\theta\right)^2 + k_2\left(-x\sin\theta + y\cos\theta\right)^2\right]. \tag{2}$$

This equation defines the surface height $z(x,y)$ relative to the local tangent plane, where k_1 and k_2 are the principal curvatures and θ denotes the orientation of their principal directions. From these principal curvatures, the Gaussian curvature is defined as their product, $K_G = k_1 k_2$. This intrinsic metric provides a rigorous criterion for classifying the local topological nature of the catalyst surface. As schematically illustrated in Figure S1, the sign of K_G distinguishes three fundamental geometric motifs: (a) elliptic regions ($K_G > 0$), where the surface curves in the same direction (synclastic), forming dome- or bowl-shaped sites; (b) parabolic or planar regions ($K_G = 0$), which correspond to cylindrical surfaces or flat facets; and (c) hyperbolic regions ($K_G < 0$), characterized by opposing principal curvatures (anticlastic) that create saddle-shaped geometries.

While (k_1, k_2, θ) fully parameterize the local curvature, they are inherently coupled. Expanding Eq. (2) yields the curvature tensor components in the (x,y) frame (k_x, k_y, k_{xy}), which can be further reorganized into a set of orthogonal angular modes via polar decomposition:

$$K_i = k_x + k_y = k_1 + k_2, \tag{3}$$

$$K_a = k_x - k_y = (k_1 - k_2)\cos 2\theta, \tag{4}$$

$$K_t = 2k_{xy} \quad = (k_1 - k_2)\sin 2\theta. \tag{5}$$

Here, k_x and k_y quantify the geometric bending along the axes aligned with the x- and y-axes, respectively. K_i represents the isotropic mean curvature, quantifying the overall magnitude of surface bending. Physically, this corresponds to a uniform breathing mode that induces average structure bending without breaking in-plane symmetry. In contrast to the isotropic term K_i, both K_a and K_t represent symmetry-breaking anisotropic distortions that contribute zero to the mean curvature. However, they capture distinct physical modes: K_a quantifies the directional disparity aligned with the intrinsic axes (x and y), representing a normal shear deformation. The mixed term K_t represents twist curvature, capturing the off-axis shear distortion that twists the local coordination environment.r

Under this framework, any intrinsic property $\mathcal{P}$ of an active site embedded in such a surface is functionally dependent on (K_i, K_a, K_t). A multivariate Taylor expansion around the planar limit ($K_i = K_a = K_t = 0$) gives the general curvature–property relationship:

$$\mathcal{P}(K_i, K_a, K_t) = \mathcal{P}_0 + \sum_{j\in\{i,a,t\}} c_j\, K_j + \frac{1}{2} \sum_{j,l\in\{i,a,t\}} H_{jl}\, K_j K_l + \mathcal{O}(K^3), \tag{6}$$

where $c_j = (\partial\mathcal{P}/\partial K_j)_0$ are the linear geometric susceptibilities and $H_{jl} = (\partial^2\mathcal{P}/\partial K_j \partial K_l)_0$ are the elements of the geometric Hessian, with $j, l \in \{i, a, t\}$. This expansion is model-agnostic: the geometric structure (orthogonal modes and their coupling pattern) is universally dictated by differential geometry, while all material-specific information is encoded in the response coefficients (c_j, H_{jl}, etc.).

The functional form of Eq. (6) is further constrained by the point-group symmetry of the active site. For the M–N_4 moiety (D_{2h}), the twist mode K_t is antisymmetric under vertical mirror reflections, which requires all odd-order terms in K_t—including the linear coefficient c_t and all mixed terms of the form K_t^{2n+1}—to vanish identically (Note S1.4). This is an exact selection rule, independent of curvature magnitude. The leading contribution of K_t therefore enters only at second order ($\propto K_t^2$). Furthermore, in the small-curvature limit, where the second-order and higher terms become negligible, this further simplifies to the

linear geometric descriptor:

$$\varphi = c_i\, K_i + c_a\, K_a. \tag{7}$$

Thus, the combination of symmetry selection and linearization reduces the general expansion (Eq. (6)) from a multi-term tensor series to a two-parameter scalar. The framework is valid for continuous geometric modulations where the local curvature varies smoothly; it is not intended to describe abrupt topological defects or structural singularities at which differentiability breaks down.

Construction of the Curvature-Defined Structural Library

Applying this formalism to the Fe–N_4–C system as a primary case study, we constructed a systematic library of curved structures by geometrically projecting a planar, hydrogen-passivated graphene sheet embedding a Fe–N_4 moiety onto analytically defined quadratic surfaces (Figure S2). This projection procedure enables controlled and independent variation of the three geometric parameters (k_1, k_2, θ), thereby providing a well-defined curvature space for systematic exploration. Previous studies have demonstrated that cluster models reproduce qualitative trends and dopant-dependent reactivity patterns in SACs.[59–61] Since our objective is to establish curvature–property scaling based on relative energetic modulation across geometries, this modeling strategy is appropriate. In the defined coordinate system, the x- and y-axes symmetrically bisect the six- and five-membered rings, respectively (Figure 1). During structural relaxation, the carbon scaffold was constrained to preserve the imposed curvature field (Figure S3(a)), while allowing the Fe–N_4 moiety and adsorbates to fully relax (details in Note S2).

To establish the physically relevant curvature regime, we analyzed the surface topology of amorphous carbon generated from molecular dynamics simulations, with curvature statistics evaluated on the sp^2 framework (see Note S3). The simulated support is predominantly composed of sp^2-hybridized carbon (92.9%), and root-mean-square deviation analysis

confirms that the graphitic scaffold remains dynamically stable throughout the trajectory, with fluctuations of merely 0.22 Å (Figure S4(a)–(d)). The mean curvature ($K_i/2$) displays a narrow, symmetric distribution centered near zero, with 81.9% of the surface area confined within ± 0.12 Å^{-1} (i.e., $|K_i| \leq 0.24$ Å^{-1}; Figure S4(e)). This range is fully consistent with experimentally reported local curvatures of 0.00–0.09 Å^{-1} in porous carbon supports,[28] confirming that our parameter space reflects realistic structural fluctuations. Within this experimentally validated regime, Gaussian-curvature analysis reveals that 76.7% of the active sp^2 surface exhibits negative Gaussian curvature ($K_G < 0$), demonstrating that saddle-shaped, anisotropic geometries are the dominant topological motif in amorphous carbon frameworks (Figure S4(f)). Notably, such biaxial saddle configurations are intrinsically absent from prevailing theoretical models that approximate curvature using one-dimensional (carbon nanotubes, $K = 0$) or strictly isotropic (spherical fullerenes, $K > 0$) constructs, thereby omitting the majority curvature state realized in practical supports.

Within this physically relevant regime, k_1 and k_2 were systematically sampled in 0.02 Å^{-1} increments (Figure S5(a)), and θ was varied from 0 to $\pi/2$ (the irreducible domain defined by Fe–N_4 symmetry) in steps of $\pi/12$ (Figure S5(b)), initially defining 1,183 curved geometries. In planar Fe–N_4–C, the upper and lower surfaces are equivalent due to horizontal mirror symmetry (σ_h); however, curvature breaks this symmetry, creating electronically distinct convex and concave faces. While this ostensibly doubles the adsorption configurations to 2,366, the geometric symmetry of the quadratic form dictates that a configuration on the lower surface $(k_1, k_2, \theta, \text{bottom})$ is physically mapped to its mirror image on the upper surface $(-k_1, -k_2, \theta, \text{top})$. Accordingly, all adsorbates in this work were positioned above the Fe site on the upper surface. After exploiting additional geometric equivalences (principal-axis permutation and spherical isotropy; Figure S6 and Note S4), the dataset was rigorously reduced to 602 unique adsorption sites, forming the complete library used in this study.

Curvature-Driven Activity Landscape

To quantify how local curvature influences catalytic performance, we computed the complete Gibbs free-energy profiles for the CO_2RR on 602 non-equivalent Fe–N_4–C sites at a potential of -0.8 V vs. SHE, a typical experimental condition, using VASPsol++[52] within the constant-potential method. The reaction proceeds via the initial adsorption of CO_2, followed by sequential hydrogenation to form *COOH and *CO intermediates, and finally the desorption of product CO (adsorption configurations illustrated in Figure 2(a)):

$$^* + \mathrm{CO_2(g)} \rightarrow {}^*\mathrm{CO_2}, \tag{8}$$

$${}^*\mathrm{CO_2} + (\mathrm{H^+ + e^-}) \rightarrow {}^*\mathrm{COOH}, \tag{9}$$

$${}^*\mathrm{COOH} + (\mathrm{H^+ + e^-}) \rightarrow {}^*\mathrm{CO} + \mathrm{H_2O(g)}, \tag{10}$$

$${}^*\mathrm{CO} \rightarrow {}^* + \mathrm{CO(g)}. \tag{11}$$

The rate-determining step, characterized by the maximum Gibbs free-energy change ($\Delta G_{\max}$), was employed as the overall activity descriptor. This thermodynamic framework is well established for CO_2-to-CO electrocatalysis on M–N_4 sites, including the potential considered here (-0.8 V vs. SHE), where key elementary barriers are often reasonably approximated by the corresponding reaction free energies.[50,51]

Systematic variation of the principal curvatures (k_1, k_2) and orientation angle (θ) reveals that local curvature enables continuous tuning of the adsorption free energies of *CO_2, *COOH, and *CO over broad ranges of 0.58, 0.74, and 0.76 eV, respectively (Figure 2(b)). Crucially, linear scaling relationships persist across all sites (Figure 2(c–d) and S7). Notably, the correlation between *CO_2 and *CO ($R^2 = 0.86$) is stronger than that between *COOH and *CO ($R^2 = 0.67$), hinting at a differential sensitivity of these intermediates to local curvature. The symmetric adsorption geometry of *CO renders it the most robust representative metric for this analysis. The symmetric adsorption geometry of *CO renders its adsorption free energy the most robust descriptor for correlating curvature with catalytic activity. Con-

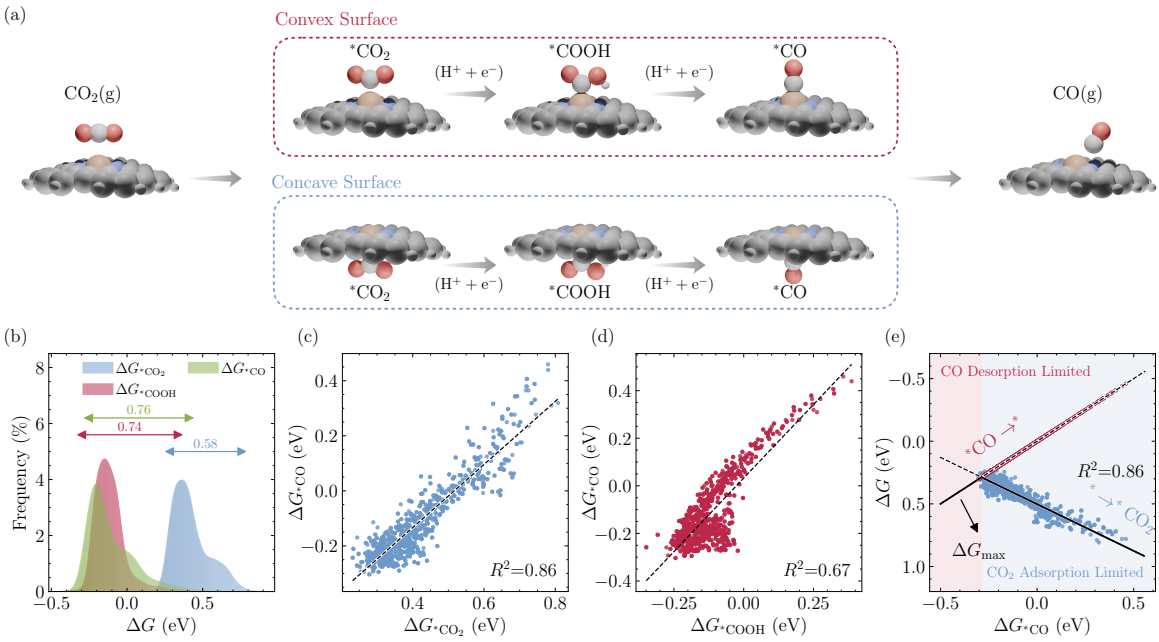

Figure 2: (a) Optimized adsorption configurations of the key reaction intermediates (*CO_2, *COOH, and *CO) on the curved Fe–N_4–C. (b) Probability density distributions of the adsorption free energies for *CO_2, *COOH, and *CO across all computed active sites. Linear scaling relationships between the adsorption free energies of (c) the *CO_2 and *CO intermediates; (d) the *COOH and *CO intermediates. (e) Sabatier volcano plot correlating the maximum Gibbs free-energy change (ΔG_{max}) with ΔG_{*CO} as the activity descriptor. The activity is governed by the lower envelope of the scaling relations for CO_2 activation and CO desorption.

sequently, plotting the reaction free energies of the two potential rate-determining steps (i.e., CO_2 activation and CO desorption) against ΔG_{*CO} reveals a clear Sabatier volcano relationship (Figure 2(e)). The catalytic activity is governed by ΔG_{max}, which follows the lower envelope of these competing trends, reflecting the fundamental trade-off between the two processes. The other two potential-dependent protonation steps remain thermodynamically favorable at −0.8 V vs. SHE (Figure S8).

As anticipated, k_1, k_2, and θ are intrinsically coupled. Projecting this orderly chemical response back onto the raw geometric coordinates reveals a chaotic landscape. As shown in Figure 3(a), the *CO adsorption energy landscape defined by (k_1, k_2, θ) appears highly convoluted. Quantitative analysis via quadratic fitting confirms this intricacy (Figure 3(b), S9 and Table S1), revealing erratic gradients and non-monotonic orientation dependencies. This demonstrates that the raw curvature parameters (k_1, k_2, θ) fail to serve as intuitive physical descriptors.

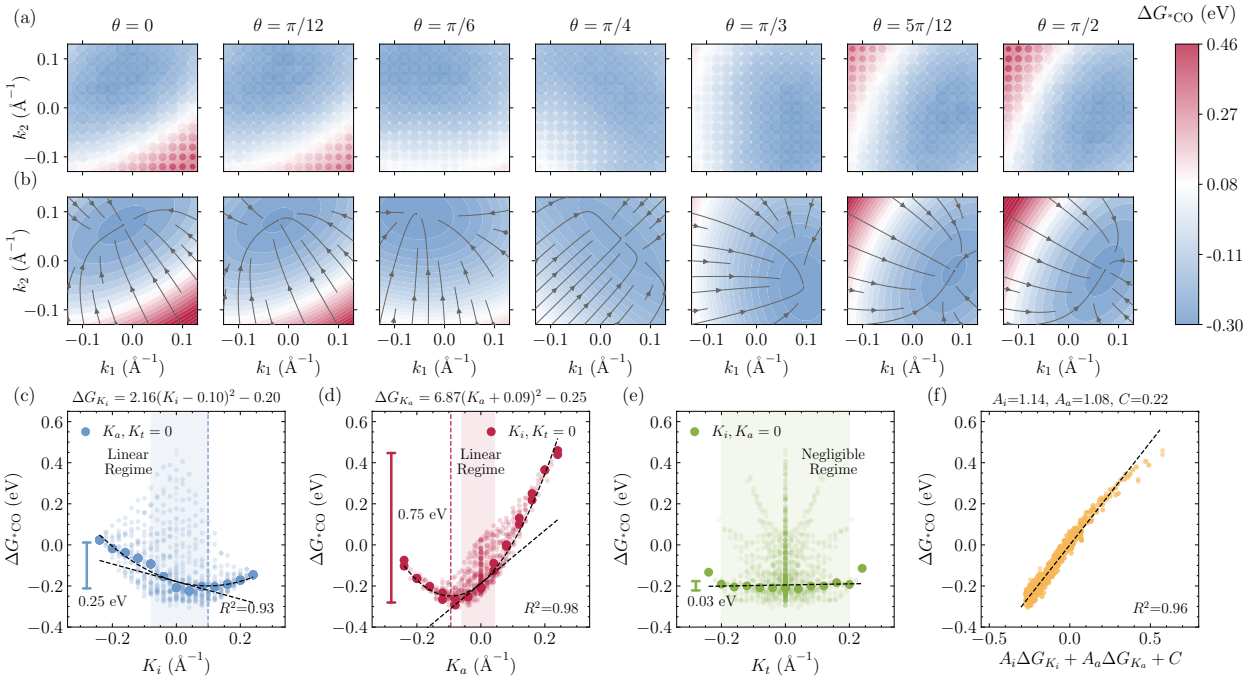

Figure 3: (a) Calculated *CO adsorption free energy ($\Delta G_{*\mathrm{CO}}$) as a function of the principal curvatures (k_1, k_2) at a fixed orientation angle θ. (b) Heatmap of the $\Delta G_{*\mathrm{CO}}$ landscape from (a) fitted by a quadratic function of k_1 and k_2. The arrows represent the gradients derived from this fitted surface, indicating the direction of strongest adsorption. (c) Correlation between $\Delta G_{*\mathrm{CO}}$ and the isotropic curvature parameter K_i, (d) the anisotropic curvature parameter K_a and (e) the twist curvature parameter K_t. In panels (c–e), transparent markers correspond to all sampled configurations, whereas large filled markers indicate the points obtained from controlled symmetry-constrained sampling. (f) Parity plot comparing DFT-calculated $\Delta G_{*\mathrm{CO}}$ with values predicted by the multivariate linear regression model based on ΔG_{K_i} and ΔG_{K_a}.

To disentangle this landscape, we transition from the raw coordinates to the decoupled orthogonal basis (Eqs. (3)–(5)). By imposing symmetry-constrained sampling conditions to isolate individual curvature components, we obtain well-defined and robust energetic responses for the Fe–N_4 site. When sampling along the isotropic (K_i) and anisotropic (K_a) curvature modes with the remaining components fixed to zero, both modes exhibit clear parabolic dependencies fitted to the symmetry-constrained data points, with $R^2 = 0.93$ for K_i and 0.98 for K_a (Figure 3(c–d)). Despite their similar functional form, the two curvature modes lead to markedly different response amplitudes. Anisotropic curvature (K_a), which breaks the in-plane symmetry of the Fe–N_4 moiety, strongly modulates $\Delta G_{*\mathrm{CO}}$ (up to ∼0.75 eV), whereas the isotropic mode (K_i) induces a much weaker change (only ∼0.25 eV); correspondingly, the quadratic curvature response is substantially larger for K_a than

for K_i (quadratic coefficients: 6.87 vs 2.16). Meanwhile, the torsional curvature component K_t shows no statistically significant correlation with the adsorption energy (Figure 3(e)). Within the physically relevant range of $-0.20 \rightarrow 0.20$ Å^{-1}, the associated energy variation remains negligible ($\sim$0.03 eV). The vanishing of the linear response is mandated by the D_{2h} symmetry of the Fe–N_4 site, but the near-complete suppression of even the symmetry-allowed second-order response ($\propto K_t^2$) is striking—particularly given that K_a and K_t differ only by a $\pi/4$ rotation of the bending axis yet produce responses differing by more than an order of magnitude. This contrast suggests that the directional bonding topology of the coordination environment strongly dictates the curvature response, rendering purely geometric descriptions insufficient. Furthermore, the absence of mirror symmetry between opposite signs of K_i and K_a exposes the breakdown of descriptions that implicitly assume convex and concave adsorption to be related by simple sign reversal, thereby limiting the applicability of scalar descriptors such as the *d*-band center. Interestingly, beyond the well-defined individual response laws, the adsorption energy exhibits an almost additive response to the two curvature modes. The adsorption energy can be accurately reconstructed as a linear superposition of the two single-mode responses:

$$\Delta G_{*\mathrm{CO}} \approx A_i \Delta G_{K_i} + A_a \Delta G_{K_a} + C, \tag{12}$$

As shown in Figure 3(f), this simple reconstruction already captures all 602 data points with high fidelity ($R^2 = 0.96$). The fitted coefficients, $A_i = 1.14$ and $A_a = 1.07$, remain remarkably close to unity, indicating that each curvature mode contributes to the adsorption energetics almost independently. Notably, such additivity is not symmetry-enforced—the D_{2h} point group formally allows $K_i K_a$ cross-coupling—suggesting that the electronic response effectively factorizes along the two geometric channels within the explored regime.

Collectively, the orthogonal decomposition resolves the complex (k_1, k_2, θ) landscape into well-defined mode responses, revealing a clear hierarchy ($K_a > K_i \gg K_t$) and an unexpected

additivity between the two active modes. While this reconstruction captures the global curvature dependence with high fidelity, $\Delta G_{*\mathrm{CO}}$ is a composite thermodynamic observable that convolutes geometric relaxation, charge redistribution, and bond reorganization, and thus does not by itself expose the microscopic origin of curvature sensitivity. To rigorously validate our geometric formalism and transcend this phenomenological description, we must bypass this complex energetic convolution and identify a fundamental intrinsic structural–electronic response.

Electronic Origin: d-Orbital Polarization

We begin by examining whether the curvature response can be rationalized by conventional energy-level-based mechanisms. The Fe center in the planar Fe–N_4 motif resides in an approximate $D_{2\mathrm{h}}$ ligand field, which already lifts the degeneracy of the d manifold almost completely, precluding a conventional Jahn–Teller-type distortion as the driving force. Consistent with this picture, PDOS analysis at representative curvatures reveals only marginal shifts in d-orbital energies relative to the planar reference (Figure S10), indicating that, within the curvature regime explored here, bending does not induce a significant degeneracy-lifting or spin-state transition. This observation is further corroborated by the weak correlation between $\Delta G_{\max}$ and the d-orbital energy centroid, ε_d (Figure S11), defined here as the occupation-weighted average energy of the Fe 3d-projected states. Beyond this weak predictive power, ε_d is an inherently isotropic metric that averages over all orbital orientations and therefore fails to distinguish between the electronically distinct convex and concave faces of a curved active site (Figure 4(a)). Taken together, these results suggest that, at least for the present system, curvature influences reactivity through effects beyond a uniform d-orbital energy shift, underscoring the need for a descriptor that explicitly incorporates the spatial characteristics of the active site.

To decode how geometric distortion translates into binding strength, we moved beyond scalar energetic metrics to interrogate the spatial topology of the Fe frontier wavefunctions.

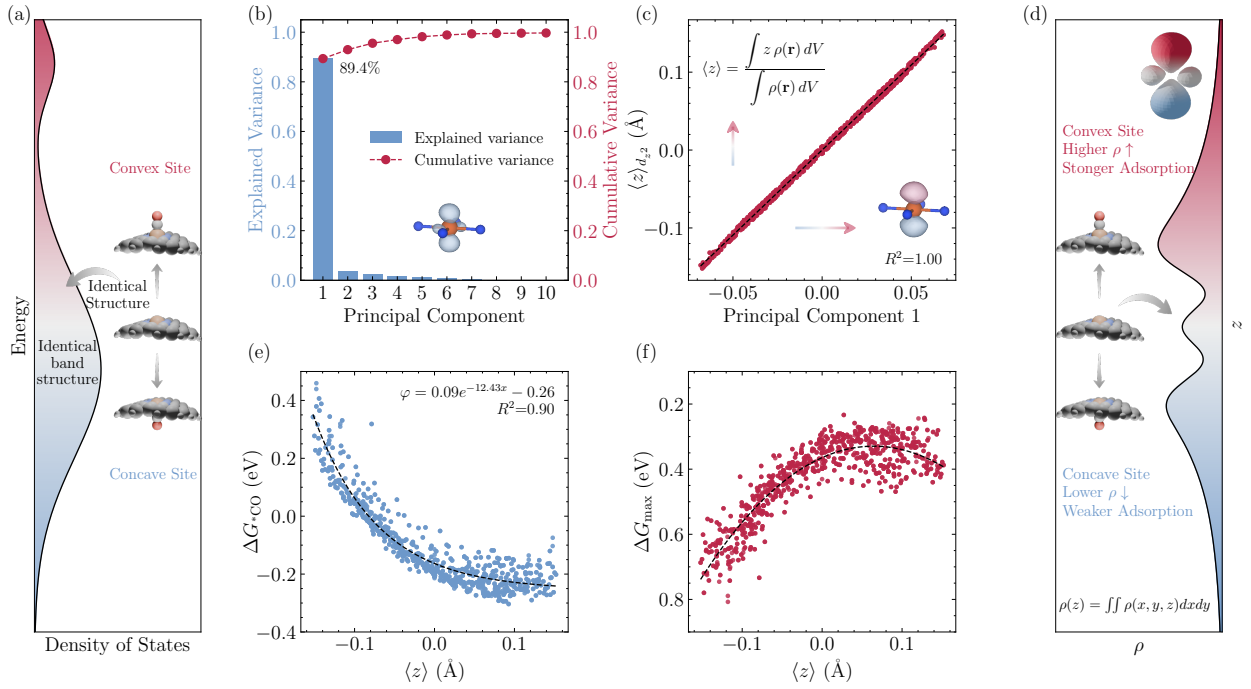

Figure 4: (a) Schematic demonstrating the inability of the d-orbital energy centroid model to distinguish between the catalytically non-equivalent upper (convex) and lower (concave) surfaces of a curved structure. (b) Variance of the d_{z^2} orbital probability density explained by each principal component and cumulative variance. (c) Visualization of the PC1 loading vector of the d_{z^2} orbital and its linear correlations with $\langle z \rangle_{d_{z^2}}$. (d) Schematic illustrating that curvature induces an asymmetric polarization of the d-orbital density (ρ) along the z-axis. Higher electron density accumulation on the adsorption side facilitates orbital overlap, leading to stronger binding, whereas density depletion results in weaker adsorption. (e) Plots of the adsorption free energies for $\Delta G_{*\mathrm{CO}}$ as a function of the electronic descriptor $\langle z \rangle$. (f) Plot of catalytic activity ($\Delta G_{\max}$) against the electronic descriptor $\langle z \rangle$.

Our analysis begins by identifying the frontier orbitals that govern the Fe–CO interaction. Projected density of states (PDOS) analysis shows that the adsorbate mainly interacts with the out-of-plane orbitals (d_{xz}, d_{yz}, and d_{z^2}), while the in-plane components (d_{xy} and $d_{x^2-y^2}$) contribute negligibly (Figure S12(e)). Among them, the d_{z^2} orbital exhibits the strongest hybridization with CO, consistent with its direct alignment along the surface normal. We therefore focused on the spin-down d_{z^2} state to probe how curvature modulates its spatial distribution. Principal component analysis (PCA) of the d_{z^2} charge density across all curved configurations shows that the first principal component (PC1) captures over 89.4% of the total variance, indicating a single dominant mode of curvature-driven electronic reorganization (details in Note S5). Visualization of the PC1 loading vector reveals that curvature induces an asymmetric reweighting of the d_{z^2} orbital lobes along the surface normal (Figure 4(c)),

with opposite lobes gaining or losing density depending on curvature. This observation motivated the construction of a new electronic descriptor, $\langle z \rangle_{d_{z^2}}$, which quantifies the centroid of the orbital charge density along the z-axis:

$$\langle z \rangle_{d_{z^2}} = \frac{\int z \rho_{d_{z^2}}(\mathbf{r}) dV}{\int \rho_{d_{z^2}}(\mathbf{r}) dV}. \tag{13}$$

The $\langle z \rangle_{d_{z^2}}$ values show a perfect linear correlation with the PC1 scores ($R^2 = 1.00$), validating that $\langle z \rangle_{d_{z^2}}$ faithfully represents the physical meaning of the dominant PCA mode. Furthermore, the polarization of the d_{xz}, d_{yz}, and d_{z^2} orbitals is highly synergistic (Figure S13), allowing us to adopt $\langle z \rangle_{d_{z^2}}$ (hereafter $\langle z \rangle$) as a robust proxy for the collective response of the out-of-plane frontier orbitals. Importantly, $\langle z \rangle$ possesses an intrinsic antisymmetry with respect to the atomic plane, assigning equal and opposite values to the convex and concave sides of a single active site ($\langle z \rangle_{\text{convex}} = -\langle z \rangle_{\text{concave}}$), enabling it to correctly distinguish the electronically inequivalent convex and concave surfaces. This distinction carries direct chemical implications: a positive $\langle z \rangle$ (typical of convex sites) indicates electron density accumulation toward the adsorbate, which enhances orbital overlap and strengthens binding; conversely, a negative $\langle z \rangle$ (concave sites) signifies density depletion at the interface, weakening the interaction (Figure 4(d)). Governed by this mechanism, the adsorption energies of *CO exhibit an exponential dependence on $\langle z \rangle$ (Figure 4(e)). This functional form is consistent with the quantum-mechanical nature of orbital interactions. Because atomic wavefunctions decay exponentially in the classically forbidden region, the overlap between the metal d_{z^2} orbital and the adsorbate is expected to decrease approximately exponentially with separation, leading to a comparable distance dependence of the interaction strength.[62] The same exponential scaling holds for *CO_2 and *COOH (Figure S14), although the correlation for *COOH is noticeably weaker. This observation now explains the differential sensitivity previously noted. CO_2 adsorption preserves the local Fe spin state (μ: $2\mu_B \rightarrow 2\mu_B$), indicating weak Fe–$CO_2$ coupling; however, the activated V-shaped CO_2 still engages the

same orbital channels as CO (σ-donation into d_{z^2} and back-donation from d_{xz}/d_{yz} into CO_2 π^*), but with smaller magnitude (Figure S12(c–e)). Because the two adsorbates interact with Fe through symmetry-equivalent orbital channels, their responses to $\langle z \rangle$ are proportional, yielding a strong mutual scaling relation. COOH, by contrast, binds through a single σ-radical pairing between its unpaired carbon radical and the singly occupied d_{z^2}, as evidenced by partial spin quenching (μ: $2\mu_B \rightarrow 1\mu_B$). The absence of effective π-back-donation channels imposes an intrinsic saturation limit on the energetic response to $\langle z \rangle$, producing the weaker scaling. This mechanistic distinction implies that curvature modulates different intermediates through inequivalent electronic pathways, potentially enabling differential tuning beyond conventional linear scaling relations. Despite this adsorbate-specific modulation, the monotonic dependence on $\langle z \rangle$ persists across all intermediates, establishing a direct link between local geometry and reactivity that ultimately yields a well-defined volcano-shaped relationship (Figure 4(f)).

Mechanical Origin of the Geometric Descriptor

With $\langle z \rangle$ established as the intrinsic electronic variable that bypasses the energetic convolution identified earlier, the remaining question is mechanistic: how does macroscopic curvature encode itself into this microscopic orbital polarization? To answer this, we decompose the orbital polarization response along each orthogonal curvature mode. Under both isotropic (K_i) and anisotropic (K_a) curvature modes, $\langle z \rangle$ exhibits a strictly odd-symmetric response (Figure 5(a–b)). As the curvature magnitude increases, the response deviates from linearity and approaches saturation, accurately captured by a hyperbolic tangent function,

$$\langle z \rangle_j = B_j \tanh(\kappa_j K_j), \tag{14}$$

where B_j represents the maximum attainable saturated displacement and κ_j controls the rate at which polarization develops with increasing curvature. Quantitative fitting reveals

a pronounced hierarchy between the two modes. The anisotropic component exhibits a substantially larger saturation amplitude ($B_a \approx 0.16$) compared to the isotropic mode ($B_i \approx 0.10$), consistent with the broader displacement range observed directly from the DFT data (0.30 vs. 0.18 Å). Moreover, the magnitude of $|\kappa_a|$ (~ 7.44) slightly exceeds that of $|\kappa_i|$ (~ 6.78), indicating a steeper initial polarization response under anisotropic bending. Together, these parameters demonstrate that K_a not only produces a larger ultimate orbital displacement but also drives a more rapid buildup of axial polarization, quantitatively rationalizing its dominant role in the energy hierarchy. The near-perfect agreement with calculations ($R^2 \approx 1.00$) establishes this hyperbolic tangent form as the intrinsic nonlinear law governing curvature-induced orbital polarization, reflecting the finite deformability of the d-electron cloud. In contrast, the torsional curvature mode K_t produces no discernible response in $\langle z \rangle$ (Figure 5(c)), with correlations close to zero. This observation is fully consistent with the symmetry-mandated vanishing of the odd term.

Consistent with the approximate mode additivity of $\Delta G_{*\mathrm{CO}}$ ($R^2 = 0.96$), the underlying electronic variable $\langle z \rangle$ strictly follows a linear superposition model. Specifically, combining the isolated single-mode contributions,

$$\langle z \rangle \approx C_i \langle z \rangle_{K_i} + C_a \langle z \rangle_{K_a}, \tag{15}$$

recovers the full orbital polarization landscape with near-perfect fidelity ($R^2 = 0.99$, Figure 5(d)), with fitted coefficients $C_i = 0.90$ and $C_a = 0.91$ both close to unity. While the nonlinear tanh-type model accurately captures the saturation behavior at extreme curvatures, the linear response regime ($K \to 0$) offers a simpler and more transferable description by retaining only the first-order susceptibilities and bypassing higher-order terms that are more sensitive to the global elastic boundary conditions of the support. Therefore, by performing a first-order Taylor expansion ($\tanh(x) \approx x$), we express the polarization as a superposition

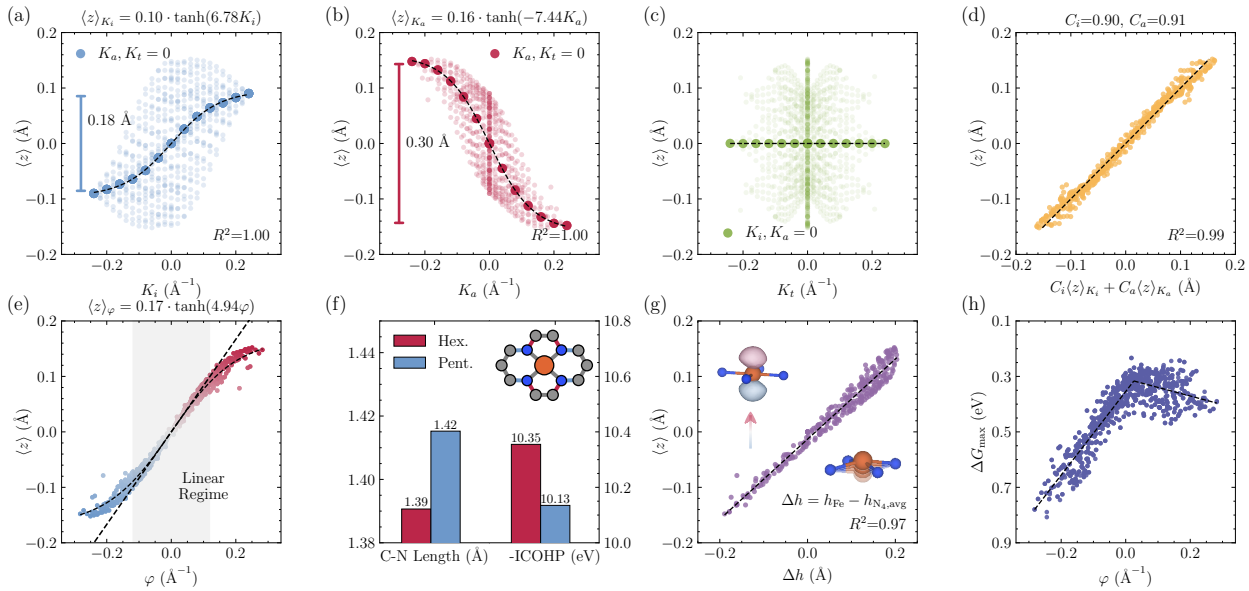

Figure 5: Correlation between $\langle z\rangle$ and (a) the isotropic (symmetric) curvature parameter K_i, (b) the anisotropic curvature parameter K_a and (c) the torsional (twist) curvature parameter K_t. In panels (a–c), transparent markers correspond to all sampled configurations, whereas large filled markers indicate the points obtained from controlled symmetry-constrained sampling. (d) Parity plot comparing $\langle z\rangle$ with values predicted by the multivariate linear regression model based on $\langle z\rangle_{K_i}$ and $\langle z\rangle_{K_a}$. (e) Plot of the electronic descriptor, $\langle z\rangle$, as a function of the geometric descriptor, φ. (f) Comparison of both bond lengths and -ICOHP values for the first and second coordination shells, analyzed along pentagonal and hexagonal ring directions across different coordination environments. (g) Structural origin of the electronic response: Linear dependence of $\langle z\rangle$ on the vertical Fe displacement (Δh). (h) Plot of catalytic activity ($\Delta G_{\max}$) against the geometric descriptor, φ.

of orthogonal geometric modes:

$$
\begin{aligned}
\varphi &\approx C_i\langle z\rangle_{K_i} + C_a\langle z\rangle_{K_a} \\
&\approx C_iB_i\tanh(\kappa_iK_i) + C_aB_a\tanh(\kappa_aK_a) \\
&\approx C_iB_i\kappa_iK_i + C_aB_a\kappa_aK_a \\
&= c_iK_i + c_aK_a,
\end{aligned}
\tag{16}
$$

where $c_j = C_jK_j\kappa_j$ denotes the intrinsic geometric susceptibility. To delineate the validity of this linear description, we systematically compare the linear prediction φ with the DFT-calculated orbital displacement $\langle z\rangle$ (Figure 5(e)). Within the curvature range $|K| < 0.11$ Å^{-1}, all data points cluster tightly around the parity line, with deviations remaining below 10%. Translating this threshold into geometric dimensions, this linear regime

corresponds to structural features with radii of curvature $R \gtrsim 9$ Å, equivalent to carbon nanotube diameters of $D > 1.8$ nm or spherical pore diameters of $D > 3.6$ nm. This range encompasses the vast majority of experimentally synthesized catalytic supports, including CNTs and the predominant fraction of mesoporous carbons, thereby confirming that the simple linear descriptor is sufficiently accurate for most practical catalyst design scenarios. At larger curvature (e.g., ultrasmall fullerenes or small-diameter CNTs), the true displacement systematically falls below the linear prediction, exhibiting a characteristic S-shaped deviation that signals the progressive involvement of higher-order nonlinear terms.

Substituting the fitted parameters yields $c_i \approx 0.58$ and $c_a \approx -1.07$ Å. The opposing signs indicate that the two curvature modes drive orbital polarization in opposite directions, while the nearly twofold disparity in magnitude ($|c_a| \approx 2|c_i|$) confirms the dominance of anisotropic distortion even in the perturbative limit. To decode the microscopic origin of this sign contrast, we project φ back onto the local bond axes (k_x, k_y) using the inverse relations:

$$\varphi = (c_i + c_a)\, k_x + (c_i - c_a)\, k_y \equiv c_x\, k_x + c_y\, k_y \approx -0.48\, k_x + 1.65\, k_y. \tag{17}$$

This decomposition reveals a striking competition: curvature along the pentagonal-ring direction (k_y) has a dominant positive coefficient ($c_y \approx 1.65$), whereas curvature along the hexagonal-ring direction (k_x) has a smaller, negative coefficient ($c_x \approx -0.48$). This implies that positive bending along the y-axis efficiently drives the electron cloud upward (increasing $\langle z \rangle$), while the same positive bending along the x-axis paradoxically pulls it downward (reducing $\langle z \rangle$), albeit less effectively. We trace this direction-dependent behavior to the contrasting mechanical stiffness of the coordination environment. Our calculations confirm that C–N bonds in the pentagonal rings are shorter (1.39 vs. 1.42 Å) and intrinsically stronger (ICOHP: 10.35 vs. 10.13 eV) than those in the hexagonal rings (Figure 5(f)). Consequently, the rigid pentagonal rings resist in-plane deformation, channeling geometric strain into a pro-

nounced out-of-plane protrusion of the metal center; in contrast, the more flexible hexagonal rings partially dissipate strain through in-plane lattice relaxation, resulting in a dampened, negative displacement. This mechanical displacement (Δh) serves as the direct structural proxy for the electronic polarization, evidenced by the precise linear scaling between $\langle z \rangle$ and Δh (Figure 5(g)). This mechanical picture also resolves the puzzling inertness of the twist mode K_t noted earlier. Since $K_t = 2k_{xy}$ is the off-diagonal component of the curvature tensor, a pure K_t deformation (with $K_i = K_a = 0$) implies $k_x = k_y = 0$, meaning zero net bending along either bond-axis direction. Without differential strain along the pentagonal and hexagonal rings, the mechanical driving force for vertical Fe displacement vanishes, rendering K_t incapable of producing a significant $\langle z \rangle$ response. Armed with this physically grounded descriptor, we finally resolve the geometric complexity: plotting the catalytic activity ($\Delta G_{\max}$) against φ consolidates the entire 602-point landscape onto a single, pristine volcano (Figure 5(h)), validating φ as the unified predictive coordinate for curvature-driven catalysis.

Generality and Design Implications of the Geometric Descriptor

To probe the transferability of these Fe–N_4-derived parameters, we systematically expanded our validation across three independent dimensions. For these tests, a representative subset of 40 curved configurations spanning the full φ range and diverse curvature morphologies (spherical, cylindrical, and saddle-shaped surfaces) was selected from the cluster library (Table S2), supplemented by carbon nanotubes of varying diameters and chiralities (Table S4) and uniaxially strained graphene supercells (Table S3).

We first examined systems that preserve the D_{2h} symmetry of the binding site but vary in chemical identity. As shown in Figure 6(a–b), when the metal center is substituted (Mn, Co, Ni) or the adsorbate is varied (*OH, *H, *N), the adsorption free energies maintain a monotonic dependence on the original φ. Since the geometric driving force remains constant, the chemical identity of the metal or adsorbate merely modulates the baseline interaction

strength (intercept) and electronic sensitivity (slope) without altering the fundamental scaling law.

Even more strikingly, this robustness extends to coordination environments that break the original symmetry, such as N_3C, N_3V, and the distinct N_2C_2 isomers (parallel, vertical, and diagonal configurations, denoted as N_2C_{2p}, N_2C_{2v}, and N_2C_{2d}, respectively; Figure 6(c)). Despite significant variations in local bonding topology, these structures adhere to the same fundamental scaling trend without the need for recalibration. Bonding analysis reveals the structural origin of this transferability: across all coordination environments, the bonds linking first-shell atoms to five-membered rings are consistently shorter and exhibit larger $-$ICOHP values than those connected to six-membered rings (Figure S15(b–c)). This indicates that the differential mechanical stiffness is rooted in the pentagon–hexagon ring contrast of the carbon scaffold and remains intact despite compositional modifications in the first coordination sphere.

Beyond compositional and local structural variations, we compared the *CO adsorption energies computed in vacuum and at -0.8 V vs. SHE to test the robustness of the scaling under different computational conditions. As shown in Figure 6(d), the monotonic scaling with φ is robustly maintained in both cases. In addition, the energetic deviation between the two conditions is asymmetric—minimal at negative φ (concave sites) and progressively widening at positive φ (convex sites)—consistent with the directional nature of the curvature-induced orbital polarization: convex sites concentrate d-electron density at the binding interface, amplifying the local dipole and hence the Stark-effect susceptibility, whereas concave sites polarize density away from the adsorbate, leaving the interaction relatively field-insensitive.

To further probe the robustness of φ, we tested partially constrained cluster models (only the outermost carbon ring fixed; Figure S3(b)) and unconstrained fully periodic models (strained graphene supercells and carbon nanotubes). All three modeling strategies preserve the monotonic φ–adsorption energy scaling (Figure 6(e) and S16). In the partially constrained clusters, larger scatter appears at high curvatures where partial relaxation allows

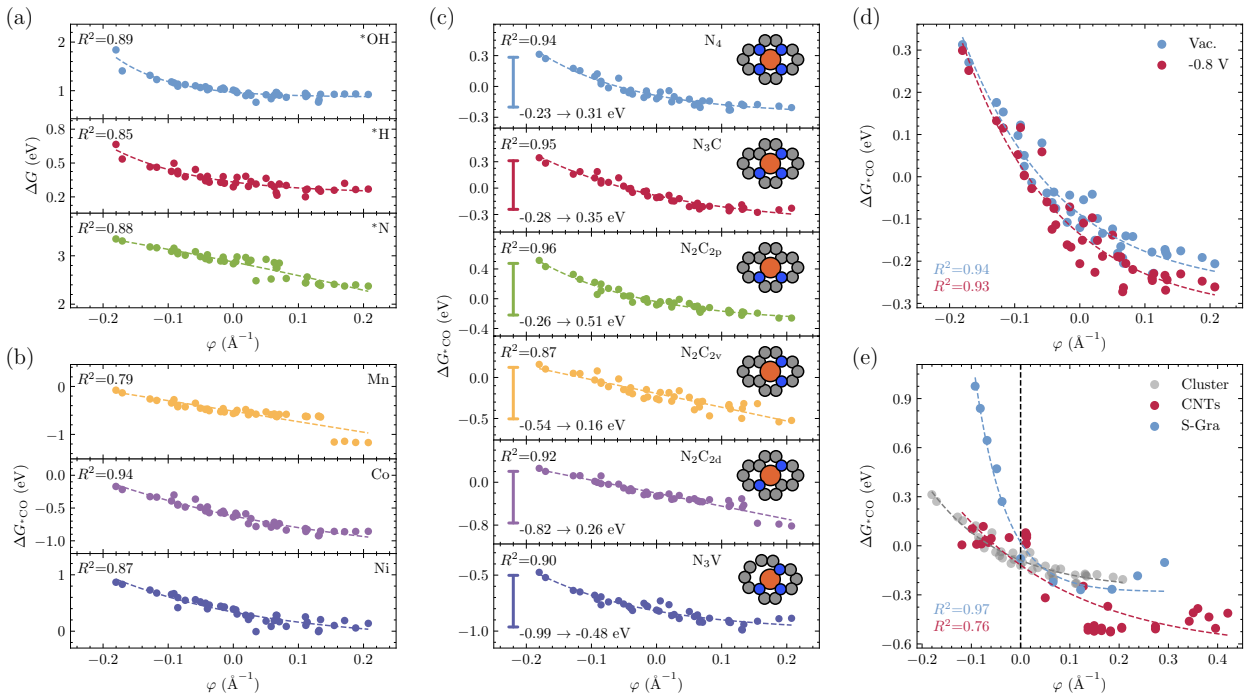

Figure 6: Universality of the geometric descriptor φ. (a) Adsorption free energies of diverse intermediates (*OH, *H, *N) on Fe–N_4–C as a function of φ. (b) Adsorption free energies of *CO on M–N_4–C (M = Mn, Co, Ni) as a function of φ. (c) Adsorption free energies on Fe sites with distinct first-shell coordination environments (N_4, N_3C, N_2C_{2p}, N_2C_{2v}, N_2C_{2d}, and N_3V) as a function of φ. (d) ΔG_{*CO} on Fe–N_4–C computed under vacuum and under an applied electrochemical potential of -0.8 V vs. SHE as a function of φ. (e) ΔG_{*CO} as a function of φ for uniaxially strained graphene (strain along the x- and y-directions), carbon nanotubes of varying diameters and chiral indices, and their overlay with the cluster library data, demonstrating a universal scaling relation across diverse structural motifs.

the local geometry to deviate from the imposed value, yet the underlying trend remains intact. Strained graphene, with its well-defined periodic boundary conditions, yields a particularly clean quantitative correlation. CNTs present the most complex case: the chiral index simultaneously determines the embedding orientation (θ) of the active site and imposes commensurability constraints that alter the supercell size and electronic character (metallic vs. semiconducting); despite this intrinsic heterogeneity, the CNT data still follow the same monotonic trend. A clear hierarchical pattern emerges from this collective comparison: near the planar limit ($\varphi \approx 0$) all models nearly coincide, reflecting a shared reference state governed by the local Fe–N_4 chemistry, whereas at higher $|\varphi|$ the curves progressively diverge into system-dependent branches as the global mechanical response of each host lattice modulates the quantitative baseline. Thus, φ functions as a transferable geo-

metric driving coordinate within each structural framework, while quantitative comparison across distinct modeling environments requires accounting for their specific electronic and mechanical contexts. Finally, preliminary CI-NEB calculations on a representative subset of curved structures show that the activation barrier of the *COOH $\rightarrow$ *CO dissociation step also exhibits a monotonic dependence on φ (Figure S17), indicating that the same geometric variable governing thermodynamics extends to kinetic barriers.

Notably, this unified framework rationalizes a wide breadth of previous theoretical and experimental observations by rigorously recovering their specific geometric conditions as limiting cases. For instance, the linear curvature–adsorption correlations reported for carbon nanotubes (uniaxial limit, $k_2 = 0$)[35–39] and spherical carbon supports (isotropic limit, $k_1 = k_2$)[23] are naturally derived from our general descriptor φ, which simplifies to $\varphi \propto k$ under these high-symmetry constraints. This proves that these earlier models were probing specific, simplified slices of the complete geometric parameter space. Crucially, by incorporating the full curvature tensor, our model resolves apparent inconsistencies in the literature regarding the directionality of the effect. A striking example is the contrast between Zhao et al., who observed that bending along the armchair direction (hexagonal axis) weakens adsorption,[36–38] and Ma et al., who reported that bending along the zigzag-like direction (pentagonal axis) significantly strengthens it.[39] Our framework quantitatively unifies these seemingly contradictory observations: they correspond precisely to the opposing signs of our derived coefficients ($c_x < 0$ vs. $c_y > 0$), confirming that the anisotropic mechanical response is the hidden variable governing these diverse trends.

Beyond rationalizing existing data, our framework highlights a critical geometric constraint for the forward-looking design of catalyst morphologies. For CNTs, our descriptors reveal that controlling the macroscopic diameter alone is insufficient to guarantee uniform catalytic performance. As shown in Figure S18, the chirality-dependent orientation of the active sites leads to a scenario where experimentally consistent diameters actually host a wide distribution of intrinsic activities. This signifies that the geometric alignment (θ) of the

Fe–N_4 axis relative to the curvature vector is as critical as the curvature magnitude itself. Consequently, rational design strategies targeting high-performance CNT-based catalysts must account for this intrinsic heterogeneity, recognizing that distinct chiralities—even with identical diameters—can yield significantly divergent thermodynamic limiting potentials.

More broadly, we note that planar M–N–C models frequently predict weak or even unfavorable initial CO_2 activation, yet many experimentally realized M–N–C catalysts—which are typically supported on curved carbon frameworks—exhibit appreciable CO_2RR activity. While multiple factors likely contribute to this discrepancy, the curvature-induced enhancement of CO_2 activation identified here may be one of them. Separately, in macroscopic experiments—such as the porous carbon supports synthesized by Wang et al.[28]—a broad statistical distribution of local curvatures may increase the probability of accessing near-optimal activity regimes, thereby enhancing the overall catalytic performance. Although moving beyond this statistical probability to deterministic control remains challenging, emerging synthesis strategies—exemplified by precise biaxially strained arrays[63] or template-assisted curvature engineering—suggest that such control is increasingly feasible.

Conclusions

In summary, we have established a geometric framework grounded in differential geometry and a symmetry-constrained Taylor expansion to quantify the impact of surface curvature on single-atom catalysis. By decomposing the local topology of any smooth surface into orthogonal curvature modes—isotropic (K_i), anisotropic (K_a), and torsional (K_t)—and applying symmetry selection rules together with a small-curvature linear approximation, we derived the scalar geometric descriptor $\varphi = c_i K_i + c_a K_a$. Instantiating this formalism for Fe–N_4–C SACs, we demonstrate that φ maps the multidimensional CO_2RR landscape of 602 nonequivalent curved sites into a predictive volcano relationship. The underlying electronic origin is an asymmetric out-of-plane d-orbital polarization along the surface normal, quantified

by the out-of-plane centroid of the d orbital, $\langle z \rangle$. We trace this polarization to its mechanical origin: the intrinsic stiffness contrast between pentagonal and hexagonal rings channels geometric strain into opposite vertical displacements of the metal center, establishing a causal pathway—Geometry (φ) $\rightarrow$ Mechanics (Stiffness) $\rightarrow$ Electronics ($\langle z \rangle$) $\rightarrow$ Activity ($\Delta G_{\max}$).

The robustness of this framework is demonstrated across multiple independent dimensions: diverse metal centers, reaction intermediates, coordination environments that break the original symmetry, periodic models, and applied electrochemical potential conditions. Moreover, by recovering previous uniaxial and isotropic models as mathematical limiting cases, the framework rationalizes reported inconsistencies in the literature regarding the directionality of curvature effects, indicating anisotropic mechanical response as a key governing factor. While realistic materials inevitably introduce environment-specific structure and electronic renormalizations, the persistence of a monotonic response to φ across all tested scenarios supports that curvature engineering is a practical design axis complementary to conventional electronic-structure tuning.

We note that the present analysis is grounded in a thermodynamic descriptor framework; a systematic extension to explicit, potential-dependent activation barriers represents an important future direction. We anticipate that continued advances in synthetic control of well-defined curvature fields will transform curvature from a statistical consequence of morphology into a controllable parameter in catalyst design.

Acknowledgement

This work is supported by National Natural Science Foundation of China (22073076 and 21933009), and the Fundamental Research Funds for the Central Universities of China (20720240138). We sincerely thank Associate Professor Maoyuan Wang for fruitful discussions and valuable theoretical guidance. The Xiamen University's High-Performance Computing Center and the State Key Laboratory Chemistry of Solid Surfaces at the Xiamen

University are acknowledged for the supercomputer resources. Shaorong Fang and Tianfu Wu from Information and Network Center of Xiamen University are acknowledged for the help with the GPU computing.

Supporting Information

See the supplementary material for the rigorous theoretical derivation of the universal geometric descriptor based on symmetry-constrained Taylor expansion (Note S1). It provides detailed methodologies for the geometric construction of curved models (Note S2) and the molecular dynamics simulation protocols[64–66] (Note S3). Furthermore, it describes the symmetry-based dataset reduction strategy (Note S4), the principal component analysis (PCA) of *d*-orbital wavefunctions (Note S5), and computational details for the generality and robustness validation calculations (Note S6). Additional data include validation of the quadratic fitting and projected density of states (PDOS) analysis.

The code for structure generation, wavefunction analysis, and the calculation of the geometric descriptor $\langle z \rangle$ is available at `https://github.com/Migie-cphy/Curvature-Driven-Catalysis`. The dataset, including DFT input/output files and exported orbital densities, is archived on Zenodo (DOI: 10.5281/zenodo.18823122).

References

(1) Wei, N.; Ding, Y.; Zhang, J.; Li, L.; Zeng, M.; Fu, L. Curvature geometry in 2D materials. *National Science Review* **2023**, *10*, nwad145.

(2) Chen, C.; Zhang, Z.; Dai, L.; Li, B.; Li, Z. High-curvature single-atom catalysts for electrocatalysis: a review. *Applied Catalysis A: General* **2025**, *694*, 120160.

(3) Yang, X.-F.; Wang, A.; Qiao, B.; Li, J.; Liu, J.; Zhang, T. Single-atom catalysts:

a new frontier in heterogeneous catalysis. *Accounts of Chemical Research* **2013**, *46*, 1740–1748.

(4) Wang, A.; Li, J.; Zhang, T. Heterogeneous single-atom catalysis. *Nature Reviews Chemistry* **2018**, *2*, 65–81.

(5) Wang, Y.; Wang, D.; Li, Y. Rational design of single-atom site electrocatalysts: from theoretical understandings to practical applications. *Advanced Materials* **2021**, *33*, 2008151.

(6) Li, M.; Wang, H.; Luo, W.; Sherrell, P. C.; Chen, J.; Yang, J. Heterogeneous single-atom catalysts for electrochemical CO_2 reduction reaction. *Advanced Materials* **2020**, *32*, 2001848.

(7) Giulimondi, V.; Mitchell, S.; Pérez-Ramírez, J. Challenges and opportunities in engineering the electronic Structure of single-atom catalysts. *ACS Catalysis* **2023**, *13*, 2981–2997.

(8) Gao, X.; Huang, G.; Jing, S.; Xu, S.; Xue, Z. Z.; Wang, L.; Li, N. Strategies for enhancing catalytic performance of single-atom catalysts in $2e^-$ oxygen reduction reaction: a review. *The Innovation Materials* **2025**, *3*, 100141.

(9) Gao, M.; Skolnick, J. A comprehensive survey of small-molecule binding pockets in proteins. *PLoS Computational Biology* **2013**, *9*, e1003302.

(10) Xu, W.; Wu, Y.; Gu, W.; Du, D.; Lin, Y.; Zhu, C. Atomic-level design of metalloenzyme-like active pockets in metal–organic frameworks for bioinspired catalysis. *Chemical Society Reviews* **2024**, *53*, 137–162.

(11) Kroto, H. W.; Heath, J. R.; O'Brien, S. C.; Curl, R. F.; Smalley, R. E. C60: Buckminsterfullerene. *Nature* **1985**, *318*, 162–163.

(12) Iijima, S. Helical microtubules of graphitic carbon. *Nature* **1991**, *354*, 56–58.

(13) Mackay, A. L.; Terrones, H.; Fowler, P. W. Hypothetical graphite structures with negative gaussian curvature. *Philosophical Transactions of the Royal Society of London. Series A: Physical and Engineering Sciences* **1997**, *343*, 113–127.

(14) Braun, E.; Lee, Y.; Moosavi, S. M.; Barthel, S.; Mercado, R.; Baburin, I. A.; Proserpio, D. M.; Smit, B. Generating carbon schwarzites via zeolite-templating. *Proceedings of the National Academy of Sciences* **2018**, *115*, E8116–E8124.

(15) Xia, Y.; Sun, W.; Yang, Q.; Jiang, L.; Wang, Y.; Hu, Y.; Chen, F. Saddle-shaped chiral nanographenes embedded with dipleiadiene and thia[6]helicene units. *Organic Chemistry Frontiers* **2025**, *12*, 6980–6988.

(16) Liu, J. Catalysis by supported single metal atoms. *ACS Catalysis* **2017**, *7*, 34–59.

(17) Cui, X.; Li, W.; Ryabchuk, P.; Junge, K.; Beller, M. Bridging homogeneous and heterogeneous catalysis by heterogeneous single-metal-site catalysts. *Nature Catalysis* **2018**, *1*, 385–397.

(18) Song, W.; Xiao, C.; Ding, J.; Huang, Z.; Yang, X.; Zhang, T.; Mitlin, D.; Hu, W. Review of carbon support coordination environments for single metal atom electrocatalysts (SACs). *Advanced Materials* **2024**, *36*, 2301477.

(19) Levy, N.; Burke, S. A.; Meaker, K. L.; Panlasigui, M.; Zettl, A.; Guinea, F.; Neto, A. H. C.; Crommie, M. F. Strain-induced pseudo–magnetic fields greater than 300 tesla in graphene nanobubbles. *Science* **2010**, *329*, 544–547.

(20) Ni, Y.; Lu, Y.; Xie, W.; Chen, J. Strain engineering of single-atom catalysts for electrochemical conversion. *ChemElectroChem* **2025**, *12*, e202400535.

(21) Mavrikakis, M.; Hammer, B.; Nørskov, J. K. Effect of strain on the reactivity of metal surfaces. *Physical Review Letters* **1998**, *81*, 2819–2822.

(22) Han, G.; Zhang, X.; Liu, W.; Zhang, Q.; Wang, Z.; Cheng, J.; Yao, T.; Gu, L.; Du, C.; Gao, Y.; Yin, G. Substrate strain tunes operando geometric distortion and oxygen reduction activity of CuN_2C_2 single-atom sites. *Nature Communications* **2021**, *12*, 6335.

(23) Wang, B.; Wang, M.; Fan, Z.; Ma, C.; Xi, S.; Chang, L.-Y.; Zhang, M.; Ling, N.; Mi, Z.; Chen, S.; Leow, W. R.; Zhang, J.; Wang, D.; Lum, Y. Nanocurvature-induced field effects enable control over the activity of single-atom electrocatalysts. *Nature Communications* **2024**, *15*, 1719.

(24) Zou, H.; Shu, S.; Yang, W.; Chu, Y.-c.; Cheng, M.; Dong, H.; Liu, H.; Li, F.; Hu, J.; Wang, Z.; Liu, W.; Chen, H. M.; Duan, L. Steering acidic oxygen reduction selectivity of single-atom catalysts through the second sphere effect. *Nature Communications* **2024**, *15*, 10818.

(25) Wang, Q.; Lyu, L.; Hu, X.; Fan, W.; Shang, C.; Huang, Q.; Li, Z.; Zhou, Z.; Kang, Y.-M. Tailoring the surface curvature of the supporting carbon to tune the d-band center of Fe-N-C single-atom catalysts for zinc-urea-air batteries. *Angewandte Chemie International Edition* **2025**, *64*, e202422920.

(26) Zhao, Y. et al. Acidic oxygen reduction by single-atom Fe catalysts on curved supports. *Nature* **2025**, *644*, 668–675.

(27) Li, J.; Xia, W.; Guo, Y.; Qi, R.; Xu, X.; Jiang, D.; Wang, T.; Sugahara, Y.; He, J.; Yamauchi, Y. Surface curvature effect on single-atom sites for the oxygen reduction reaction: a model of mesoporous MOF-derived carbon. *Chemical Engineering Journal* **2023**, *477*, 146841.

(28) Wang, T.; Wang, J.; Lu, C.; Jiang, K.; Yang, S.; Ren, Z.; Zhang, J.; Liu, X.; Chen, L.; Zhuang, X.; Fu, J. Single-atom anchored curved carbon surface for efficient CO_2 electro-

reduction with nearly 100% CO selectivity and industrially-relevant current density. *Advanced Materials* **2023**, *35*, 2205553.

(29) Chen, G.; Lu, R.; Li, C.; Yu, J.; Li, X.; Ni, L.; Zhang, Q.; Zhu, G.; Liu, S.; Zhang, J.; Kramm, U. I.; Zhao, Y.; Wu, G.; Xie, J.; Feng, X. Hierarchically Porous Carbons with Highly Curved Surfaces for Hosting Single Metal FeN_4 Sites as Outstanding Oxygen Reduction Catalysts. *Advanced Materials* **2023**, *35*, 2300907.

(30) Zhou, X.; Tamtaji, M.; Zhou, W.; Iii, W. A. G.; Chen, G. DFT screening of dual-atom catalysts on carbon nanotubes for enhanced oxygen reduction reaction and oxygen evolution reaction: comparing dissociative and associative mechanisms. *Journal of Materials Chemistry A* **2024**, *12*, 28381–28389.

(31) Liu, W.; Guo, K.; Xie, Y.; Liu, S.; Chen, L.; Xu, J. High efficiency carbon nanotubes-based single-atom catalysts for nitrogen reduction. *Scientific Reports* **2023**, *13*, 9926.

(32) Cepitis, R.; Kongi, N.; Rossmeisl, J.; Vladislav Ivaništšev Surface curvature effect on dual-atom site oxygen electrocatalysis. *ACS Energy Letters* **2023**, *8*, 1330–1335.

(33) Lin, W.; Di Tommaso, D. Screening nitrogen-coordinated single atom catalysts on armchair carbon nanotubes for enhanced electrochemical CO_2 reduction to C_1 products. *ACS Catalysis* **2025**, 16463–16475.

(34) Liang, G.-H.; Liu, H.-S.; Zhang, X.-M.; Li, J.-F.; Zheng, S. Topology-based machine learning for predicting curvature effects in metal-nitrogen-carbon single-atom catalysts. *Journal of Energy Chemistry* **2025**, *105*, 608–616.

(35) Sui, H.; Guo, Q.; Xiang, M.; Kong, X.; Zhang, J.; Ding, S.; Su, Y. Theoretical insights of curvature effects of FeN_4-doped carbon nanotubes on ORR activity. *The Journal of Physical Chemistry Letters* **2024**, *15*, 8257–8264.

(36) Ma, A.; Pang, Y.; Ding, Z.; Fan, G.; Xu, H. Curvature effect of TMN_4 sites on carbon nanotube for electrochemical reduction of carbon dioxide revealed by machine learning. *Electrochimica Acta* **2025**, *537*, 146862.

(37) Zhou, X.; Jin, Z.; Zhang, J.; Hu, K.; Liu, S.; Qiu, H.-J.; Lin, X. Curvature effects on the bifunctional oxygen catalytic performance of single atom metal–N–C. *Nanoscale* **2023**, *15*, 2276–2284.

(38) Zhao, W.; Shen, S.; Zhao, Y.; Wu, T.; Ding, S.; Su, Y. Curvature-switched activity of carbon nanotube-supported single atom catalysts for the hydrogen evolution reaction. *Journal of Materials Chemistry A* **2024**, *12*, 16476–16481.

(39) Ma, N.; Zhang, Y.; Wang, Y.; Zhao, J.; Liang, B.; Xiong, Y.; Luo, S.; Huang, C.; Fan, J. Curvature effects regulate the catalytic activity of $Co@N_4$-doped carbon nanotubes as bifunctional ORR/OER catalysts. *Journal of Colloid and Interface Science* **2024**, *654*, 1458–1468.

(40) Xu, H. Bio-Inspired Curvature Engineering across the Periodic Table Tunes Hydrogen Adsorption in Single-Atom Catalysts. *The Journal of Physical Chemistry Letters* **2026**, *17*, 665–671.

(41) Wang, M.; Lin, Y.; Xiang, Y.; Sun, Y.; Zhu, Z.-z.; Wu, S.; Cao, X. Curvature Engineering of SiFe Dual-Atom Catalysts for Enhanced CO_2 Electroreduction. *The Journal of Physical Chemistry Letters* **2026**, *17*, 1227–1234.

(42) Kresse, G.; Furthmüller, J. Efficient iterative schemes for ab initio total-energy calculations using a plane-wave basis set. *Physical Review B* **1996**, *54*, 11169–11186.

(43) Kresse, G.; Furthmüller, J. Efficiency of ab-initio total energy calculations for metals and semiconductors using a plane-wave basis set. *Computational Materials Science* **1996**, *6*, 15–50.

(44) Blöchl, P. E. Projector augmented-wave method. *Physical Review B* **1994**, *50*, 17953–17979.

(45) Hammer, B.; Hansen, L. B.; Nørskov, J. K. Improved adsorption energetics within density-functional theory using revised Perdew-Burke-Ernzerhof functionals. *Physical Review B* **1999**, *59*, 7413–7421.

(46) Perdew, J. P.; Burke, K.; Ernzerhof, M. Generalized gradient approximation made simple. *Physical Review Letters* **1996**, *77*, 3865–3868.

(47) Grimme, S.; Antony, J.; Ehrlich, S.; Krieg, H. A consistent and accurate ab initio parametrization of density functional dispersion correction (DFT-D) for the 94 elements H-Pu. *The Journal of Chemical Physics* **2010**, *132*, 154104.

(48) Grimme, S.; Ehrlich, S.; Goerigk, L. Effect of the damping function in dispersion corrected density functional theory. *Journal of Computational Chemistry* **2011**, *32*, 1456–1465.

(49) Dudarev, S. L.; Botton, G. A.; Savrasov, S. Y.; Humphreys, C. J.; Sutton, A. P. Electron-energy-loss spectra and the structural stability of nickel oxide: an LSDA+U study. *Physical Review B* **1998**, *57*, 1505–1509.

(50) Vijay, S.; Gauthier, J. A.; Heenen, H. H.; Bukas, V. J.; Kristoffersen, H. H.; Chan, K. Dipole-field interactions determine the CO_2 reduction activity of 2D Fe–N–C single-atom catalysts. *ACS Catalysis* **2020**, *10*, 7826–7835.

(51) Vijay, S.; Ju, W.; Brückner, S.; Tsang, S.-C.; Strasser, P.; Chan, K. Unified mechanistic understanding of CO_2 reduction to CO on transition metal and single atom catalysts. *Nature Catalysis* **2021**, *4*, 1024–1031.

(52) Islam, S. M. R.; Khezeli, F.; Ringe, S.; Plaisance, C. An implicit electrolyte model

for plane wave density functional theory exhibiting nonlinear response and a nonlocal cavity definition. *The Journal of Chemical Physics* **2023**, *159*, 234117.

(53) Ni, A. Z.; Rettig, A.; Lee, J. Gaussian-based periodic grand canonical density functional theory with implicit solvation for computational electrochemistry. *Journal of Chemical Theory and Computation* **2025**, *21*, 10961–10970.

(54) Peterson, A. A.; Abild-Pedersen, F.; Studt, F.; Rossmeisl, J.; Nørskov, J. K. How copper catalyzes the electroreduction of carbon dioxide into hydrocarbon fuels. *Energy & Environmental Science* **2010**, *3*, 1311–1315.

(55) Studt, F.; Abild-Pedersen, F.; Varley, J. B.; Nørskov, J. K. CO and CO_2 hydrogenation to methanol calculated using the BEEF-vdW functional. *Catalysis Letters* **2013**, *143*, 71–73.

(56) Dronskowski, R.; Bloechl, P. E. Crystal orbital Hamilton populations (COHP): energy-resolved visualization of chemical bonding in solids based on density-functional calculations. *The Journal of Physical Chemistry* **1993**, *97*, 8617–8624.

(57) Nelson, R.; Ertural, C.; George, J.; Deringer, V. L.; Hautier, G.; Dronskowski, R. LOBSTER: local orbital projections, atomic charges, and chemical-bonding analysis from projector-augmented-wave-based density-functional theory. *Journal of Computational Chemistry* **2020**, *41*, 1931–1940.

(58) Wang, V.; Xu, N.; Liu, J.-C.; Tang, G.; Geng, W.-T. VASPKIT: a user-friendly interface facilitating high-throughput computing and analysis using VASP code. *Computer Physics Communications* **2021**, *267*, 108033.

(59) Jia, H.; Nandy, A.; Liu, M.; Kulik, H. J. Modeling the Roles of Rigidity and Dopants in Single-Atom Methane-to-Methanol Catalysts. *Journal of Materials Chemistry A* **2022**, *10*, 6193–6203.

(60) Jia, H.; Duan, C.; Kevlishvili, I.; Nandy, A.; Liu, M.; Kulik, H. J. Computational Discovery of Codoped Single-Atom Catalysts for Methane-to-Methanol Conversion. *ACS Catalysis* **2024**, *14*, 2992–3005.

(61) Jia, H.; Duan, C.; Terrones, G. G.; Kevlishvili, I.; Kulik, H. J. Computational Exploration of Codoped Fe and Ru Single-Atom Catalysts for the Oxygen Reduction Reaction. *448*, 116163.

(62) Ternes, M.; González, C.; Lutz, C. P.; Hapala, P.; Giessibl, F. J.; Jelínek, P.; Heinrich, A. J. Interplay of Conductance, Force, and Structural Change in Metallic Point Contacts. *Physical Review Letters* **2011**, *106*, 016802.

(63) Zhang, T.; Ye, Q.; Liu, Y.; Liu, Q.; Han, Z.; Wu, D.; Chen, Z.; Li, Y.; Fan, H. J. Data-driven discovery of biaxially strained single atoms array for hydrogen production. *Nature Communications* **2025**, *16*, 3644.

(64) Fan, Z. et al. GPUMD: a package for constructing accurate machine-learned potentials and performing highly efficient atomistic simulations. *The Journal of Chemical Physics* **2022**, *157*, 114801.

(65) Fan, Z.; Zeng, Z.; Zhang, C.; Wang, Y.; Song, K.; Dong, H.; Chen, Y.; Ala-Nissila, T. Neuroevolution machine learning potentials: combining high accuracy and low cost in atomistic simulations and application to heat transport. *Physical Review B* **2021**, *104*, 104309.

(66) Liu, Y.; Gao, T.; Xiao, Q.; Ruan, Y.; Chen, Q.; Wang, B.; Huang, J. Generalized modeling of carbon film deposition growth via hybrid MD/MC simulations with machine-learning potentials. *npj Computational Materials* **2025**, *11*, 285.

TOC Graphic

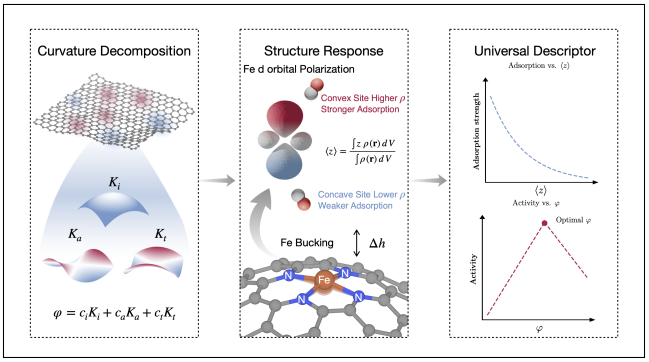
Curvature Decomposition
K_i
K_a
K_t
$\varphi = c_i K_i + c_a K_a + c_t K_t$
Structure Response
Fe d orbital Polarization
Convex Site Higher ρ
Stronger Adsorption
$\langle z \rangle = \frac{\int z\,\rho(\mathbf{r})\,dV}{\int \rho(\mathbf{r})\,dV}$
Concave Site Lower ρ
Weaker Adsorption
Fe Bucking
Δh
N
Fe
Universal Descriptor
Adsorption vs. $\langle z \rangle$
Adsorption strength
$\langle z \rangle$
Activity vs. φ
Optimal φ
Activity
φ